PHOTONICS Research

Twenty-nine million intrinsic *Q*-factor monolithic microresonators on thin-film lithium niobate

Xinrui Zhu,[1,†] Yaowen Hu,[1,2,†] Shengyuan Lu,[1] Hana K. Warner,[1] Xudong Li,[1] Yunxiang Song,[1] Letícia Magalhães,[1] Amirhassan Shams-Ansari,[1,3] Andrea Cordaro,[1] Neil Sinclair,[1] and Marko Lončar[1,*]

[1]*John A. Paulson School for Engineering and Applied Sciences, Harvard University, Cambridge, Massachusetts 02138, USA*
[2]*State Key Laboratory for Mesoscopic Physics and Frontiers Science Center for Nano-optoelectronics, School of Physics, Peking University, Beijing 100871, China*
[3]*DRS Daylight Solutions, San Diego, California 92127, USA*
[†]*These authors contributed equally to this work.*
Corresponding author: loncar@seas.harvard.edu

The recent emergence of thin-film lithium niobate (TFLN) has extended the landscape of integrated photonics. This has been enabled by the commercialization of TFLN wafers and advanced nanofabrication of TFLN such as high-quality dry etching. However, fabrication imperfections still limit the propagation loss to a few dB/m, restricting the impact of this platform. Here, we demonstrate TFLN microresonators with a record-high intrinsic quality (*Q*) factor of twenty-nine million, corresponding to an ultra-low propagation loss of 1.3 dB/m. We present spectral analysis and the statistical distribution of *Q* factors across different resonator geometries. Our work pushes the fabrication limits of TFLN photonics to achieve a *Q* factor within 1 order of magnitude of the material limit.   © 2024 Chinese Laser Press

https://doi.org/10.1364/PRJ.521172

1. INTRODUCTION

Thin-film lithium niobate (TFLN) photonics is rapidly emerging as a versatile platform for high-speed electro-optics and non-linear optics applications [1]. The material properties of lithium niobate (LN) lie at the center of this breakthrough: high refractive index, large $\chi^{(2)}$ nonlinearity, wide transparency window, and efficient piezo-electric response [2]. Recently, with commercialized TFLN wafers and advanced nanofabrication techniques based on high-quality dry etching [3], the exploration of lithium niobate photonics has been transformed from traditional bulk-scale components into integrated photonic chips, enabling both better performance and novel functionalities [1]. For example, integrated TFLN photonic devices, featuring strong nonlinear interaction, low propagation loss, and small form factors, enable significant advances in electro-optic (EO) modulation [4–6], EO frequency conversion [7], EO frequency comb generation [8–10], Kerr frequency comb generation [11–17], synthetic crystal generation [18–20], transduction [21–25], and engineered all-optical nonlinearities via periodic poling [26–30]. These components represent fundamental building blocks for advanced large-scale photonic systems, boosting applications in optical communications [31], optical computation [32], precision measurements [33], microwave signal processing [34,35], and quantum information science [36]. To unlock the full potential of the

TFLN platform, propagation loss arises as a fundamental challenge. At the device level, enhancing light–matter interaction in various applications necessitates ultra-low propagation loss, as the ratio between coupling and loss determines the strength of the desired interaction. At the system level, the requirement of integrating numerous devices to form large-scale photonic circuits is ultimately limited by loss.

Substantial research efforts have been made to minimize the propagation loss of TFLN waveguides, that is maximize the quality (*Q*) factor of TFLN resonators. Using different resonator designs [37,38], researchers have explored different etching methods to optimize fabrication quality, such as dry (ion-plasma) etching, wet etching, and chemical mechanical etching. Dry etching, utilizing reactive ion plasma, is the predominant method of etching LN [3,39–43] as it allows for precise control of feature sizes. Wet etching, though simpler, encounters the challenges of nonuniform etching along different crystal directions [44,45]. While chemical mechanical polishing yields an ultra-smooth surface, it has difficulty in preserving narrow features, thus making it hard to realize, e.g., optical waveguide coupled resonators within a single TFLN layer [46–48]. The highest *Q* factor measured in TFLN resonators realized using dry etching stands at 12 million [3,49], though even higher *Q* factors have been achieved using the CMP process [46]. However, these achievements are below the *Q* factors observed in other low-loss

photonics platforms like 442 million on the silicon nitride platform [50] and the theoretical upper limit of 163 million inherent to the TFLN platform [49]. Furthermore, most breakthrough devices exhibit average Q factors limited to a few million [7–9], restricting the overall device performance. Consequently, the Q factor remains a critical bottleneck within the TFLN platform, requiring a further push on the upper limit.

Here, we demonstrate monolithic microring racetrack resonators on the TFLN platform with a record-high intrinsic Q factor of 29.3 million, and a corresponding ultra-low propagation loss <1.3 dB/m, realized using the dry reactive ion etching. We achieve this by optimizing the fabrication process and tailoring the resonator widths and lengths to achieve the largest Q values. We evaluate the device fabrication quality using scanning electron microscopy (SEM) and atomic force microscopy (AFM). We also analyze different mode families observed in the transmission spectra of resonators, investigate the statistical relationship between the Q factor and resonator geometries, and calibrate the resonator linewidth using a radio frequency (RF) modulated laser.

2. DEVICE

Our microresonators are based on a racetrack geometry. As depicted in Fig. 1(a), the waveguide on the left can couple light in and out, and the cavity on the right is where light circulates for multiple roundtrips, experiencing the resonant enhancement. We chose the width of the racetrack section to be large, aiming for a reduced overlap between the light and sidewall. Figure 1(b) illustrates the anticipated spectrum of a ring resonator featuring

a Lorentzian-shaped resonance at the specific resonant wavelength. The Q factor can be extracted from the linewidth and wavelength mathematically. A high Q factor implies a narrow resonance linewidth and minimal propagation loss.

We fabricate high-Q resonators with an optimized fabrication process. The fabrication begins with a chip cleaved from a TFLN wafer with 600 nm thickness of LN and 4.7 µm buried silicon dioxide. The device is first patterned by electron beam lithography using 700 nm thick hydrogen silsesquioxane (HSQ) electron beam resist. We found the optimal dose to be 1600 µC/cm². The multipass writing technique is implemented to ensure high writing quality. Subsequently, approximately 325 nm of LN is etched using an inductively coupled plasma reactive ion etching tool with argon gas. 325 nm is determined to be the optimal etch depth as we observed that deeper or shallower etches result in lower Q. The dry etch process is split into two separate runs in order to check the etch rate in between (approximately 0.6 nm/s) and to reach the target etch depth. Following these steps, the device undergoes a chemical cleaning (hot potassium hydroxide, hot SC1, diluted HF, and piranha) and annealing at 520°C in oxygen gas. For wet processing we place glassware in water baths and for temperature treatment we use an LN-only annealer to avoid possible cross-contamination. This optimized fabrication method exhibits stability and repeatability in consistently yielding functional ultra-high-Q devices.

We have conducted characterizations on our racetrack resonator devices to verify the fabrication quality. Figure 1(c) presents the optical microscope image of a racetrack resonator
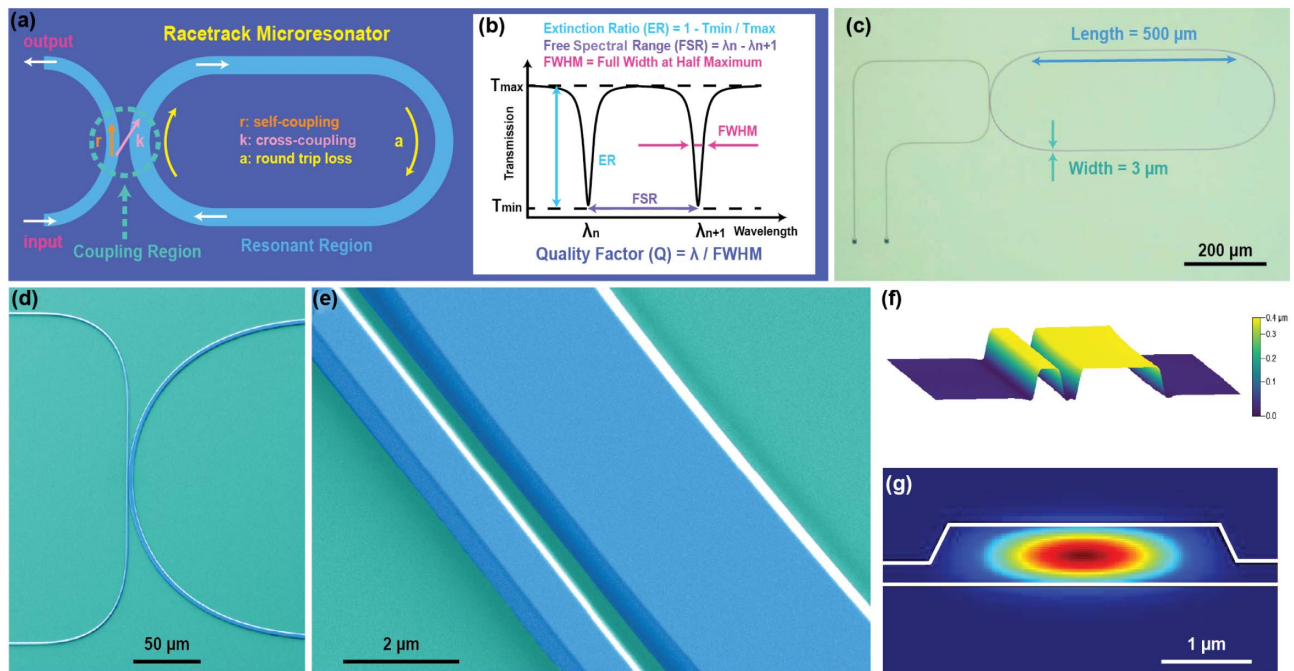
Fig. 1. TFLN microresonator with smooth sidewall. (a) Schematic illustration depicting the structure of a racetrack resonator. (b) Illustration of the transmission spectra demonstrating the characteristic features of a resonator. (c) Optical microscope image showing a racetrack resonator with 3 µm width and 500 µm length straight section. (d) SEM image (false-colored) offering an overview of the coupling region of a racetrack with 0.5 µm coupling gap and 3 µm width. (e) SEM image (false-colored) providing a detailed view of the coupling region of the same racetrack resonator. (f) AFM image capturing coupling region's topography. (g) Lumerical eigenmode simulation representing the fundamental TE mode at the cross-section of 3 µm width ring racetrack resonator.

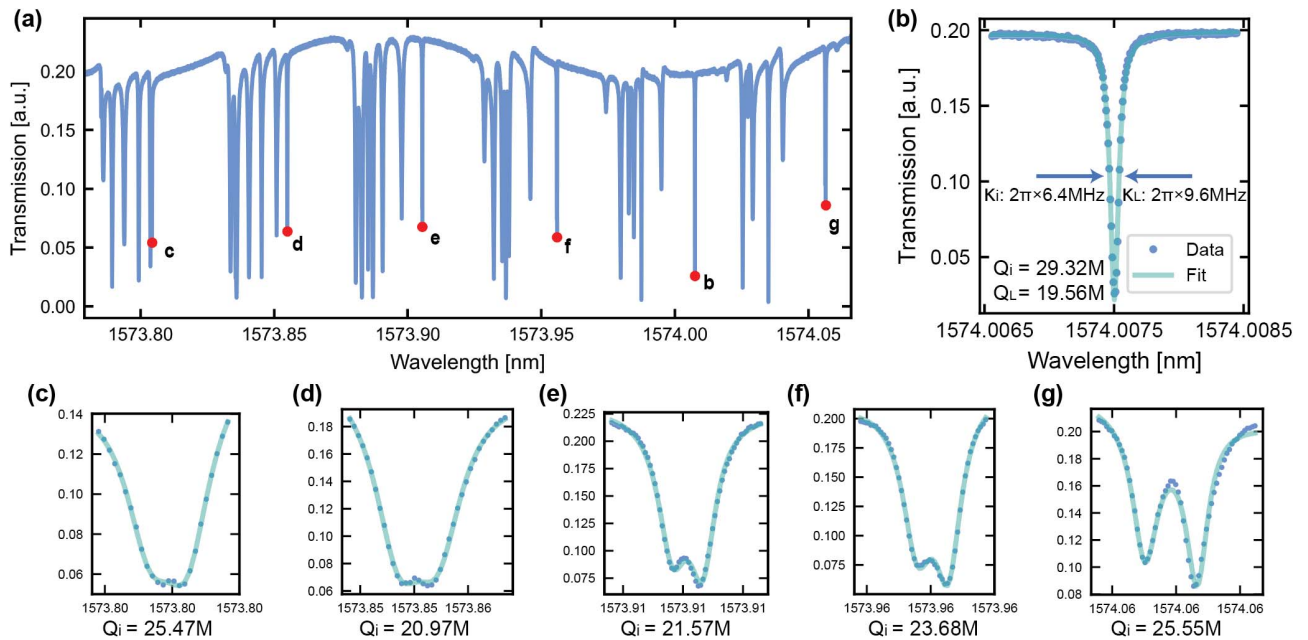with length of 500 μm and bending radius of 200 μm. Figures 1(d) and 1(e) are the SEM images of a coupling region of 3 μm width racetrack device with a coupling gap of 0.5 μm. Taken by an AFM image, Fig. 1(f) is consistent with Fig. 1(e), demonstrating the well-defined waveguide and smooth sidewalls, suggesting high fabrication quality. Additionally, Fig. 1(g), obtained from Lumerical simulation, illustrates the fundamental mode supported by a 3 μm width racetrack, showing the reduced overlap between the light and sidewall enabled by the ultra-wide waveguide. We note that wide racetrack waveguides may decrease the coupling efficiency between the bus waveguide and the resonator. Indeed, by characterizing devices with different coupling gaps, we confirmed that all resonances presented in this paper operated in the under-coupled regime. This can be attributed to the reduced overlap between the modes propagating in the coupling waveguide and resonator waveguide. To improve the coupling efficiency, as well as mitigate the excitation of higher-order modes, resonator width could be tapered down in the coupling region, or the directional or pulley coupler can be utilized [51–53].

3. MEASUREMENT

We measure our device using a tunable laser (TSL-570) and a low-noise detector (Newport 1811). Figure 2(a) demonstrates an exemplary spectrum obtained from our measurements, where the x-axis represents the wavelengths generated through laser sweep, and the y-axis denotes the signal received by the detector. The spectrum presents diverse resonance shapes featuring different linewidths and extinction ratios. This is attributed to the fact that wide racetracks support both fundamental and higher-order modes. We assigned mode family to each resonance based on their shape, extinction ratio, and free spectral range (FSR). Fundamental modes are selected by finding the mode family with the highest FSR [depicted by the red dots in Fig. 2(a)], corresponding to the minimum group index predicted by the Lumerical eigenmode simulation. We observe that the fundamental mode exhibits the highest Q factor among all the mode families (referred to as "high-Q mode family" later), which is consistent with our design as the fundamental mode typically has the smallest amount of overlap with waveguide sidewall roughness.

Many measured resonances feature ultra-high Q factors. The highest intrinsic Q factor is 29.32 million, with corresponding loaded Q factor of 19.56 million, corresponding to a device with parameters of 4.5 μm width, 10 mm length, and 0.6 μm coupling gap [Fig. 2(b)]. The intrinsic and loaded linewidths are 6.4 MHz and 9.6 MHz, respectively. The equivalent propagation loss can be calculated as $\alpha = 10\log_{10}(e^{-\kappa_i n_g L/c}) = 1.3$ dB/m, where $\kappa_i = 2\pi \times 6.4$ MHz is the intrinsic linewidth, $n_g = 2.3$ is the group refractive index, $L = 1$ m is the length, and c is the speed of light. We note that this is the upper bound for the propagation loss, since κ_i includes bending losses as well. Other resonances within the same mode family exhibit ultra-high Q values exceeding 20 million, as shown in Figs. 2(c) and 2(d). Resonances from the high-Q mode family may feature single or split peaks, which could have resulted from the mode splitting between the clockwise (CW) and counter-clockwise (CCW) modes. The typical CW and CCW mode coupling is small; however, in this ultra-high-Q regime, the linewidth could be comparable to this coupling, leading to the observation of mode splitting. In addition, the potential overlap with resonances from other mode families may also generate similar doublet features.

Fig. 2. Monolithic high-Q microresonators on TFLN. (a) Selected resonator spectrum spanning from wavelengths 1573.78 nm to 1574.06 nm. The corresponding racetrack features a width of 4.5 μm, length of 10 mm, coupling gap of 0.6 μm, and bending radius of 200 μm. Background modulation is attributed to the cavity formed by reflections between the two facets of the chip. (b) The highest-Q resonance features an intrinsic Q factor of 29 million at the wavelength of 1574 nm. (c)–(g) Resonances at wavelengths 1573.80 nm, 1573.85 nm, 1573.90 nm, 1573.95 nm, and 1574.04 nm, all belonging to the same high-Q mode family.
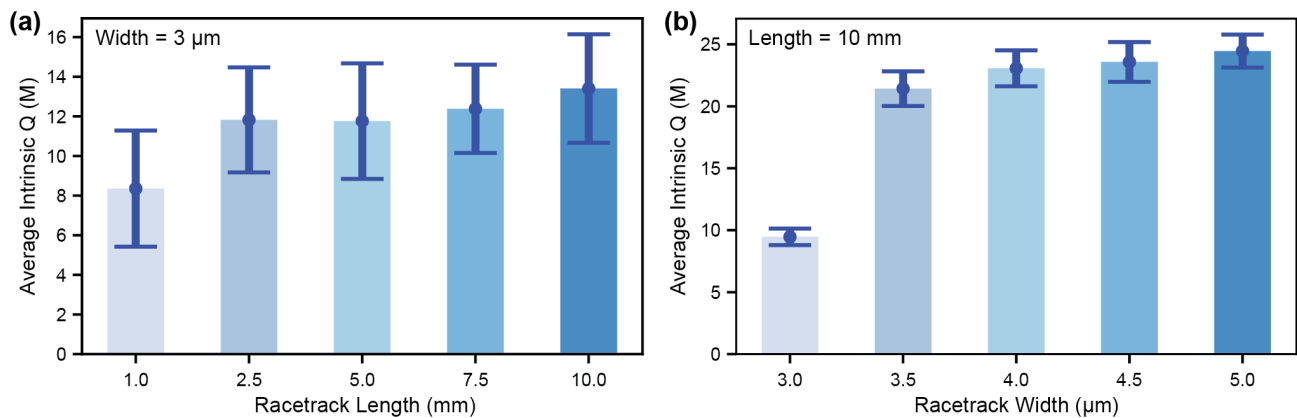
Fig. 3. Statistical analysis of intrinsic Q factor versus racetrack length and width. The bars depict the mean value of the top 50 intrinsic Q factors of a device, while horizontal marker lines are error bars, indicating the mean values plus and minus their standard deviations. (a) Average intrinsic Q of racetracks with a width of 3 μm and lengths of 1 mm, 2.5 mm, 5 mm, 7.5 mm, and 10 mm. (b) Average intrinsic Q of racetracks with a length of 10 mm and widths of 3.0 μm, 3.5 μm, 4.0 μm, 4.5 μm, and 5.0 μm.

Table 1. Data for Intrinsic Q Factor Versus Racetrack Length and Width

No.	Chip	Gap (μm)	Width (μm)	Length (mm)	Average Q (10^6)	Highest Q (10^6)	Loss (dB/m)
1	A	0.5	3.0	1.0	8.35	15.85	2.6
2				2.5	11.82	19.45	2.0
3				5.0	11.76	18.01	2.3
4				7.5	12.38	20.05	2.0
5				10.0	13.40	21.73	1.9
6	B	0.6	3.0	10.0	9.46	11.92	3.4
7			3.5		21.42	24.78	1.6
8			4.0		23.06	26.70	1.5
9			4.5		23.57	29.32	1.3
10			5.0		24.45	27.90	1.4

We perform a comprehensive statistical analysis of Q factors by examining the entire scan range of wavelengths (1480 nm to 1620 nm). For each device, an automated Python code searches for all the resonances and fits their Q values. We select the top 50 resonances from each device to represent the high-Q mode family and evaluate their average value and standard deviation. As illustrated in Fig. 3, we compare the statistical Q result for devices with different geometry. For the devices with 3 μm width, we vary the length from 1 mm to 10 mm, revealing an increasing Q trend. In the devices with 10 mm length on another chip, the Q increases as the waveguide width increases from 3 μm to 5 μm. While we extract our highest Q record from a racetrack with 4.5 μm width and 10 mm length, the average Q values of the device with 5 μm width and 10 mm length are slightly better. Furthermore, the two chips for Figs. 3(a) and 3(b) are made in two individual fabrication rounds, affirming the reproducibility of our high Q results. A summary is provided in Table 1.
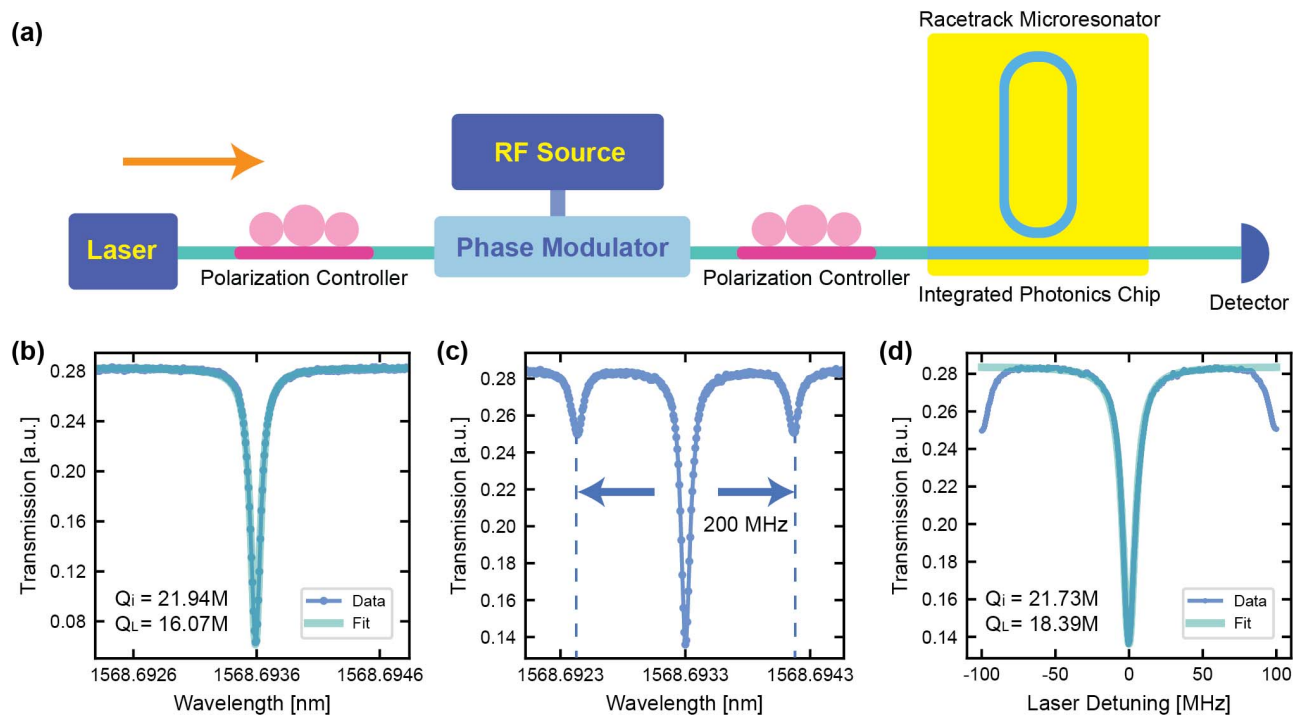
4. CALIBRATION

To verify that the direct laser sweep approach can characterize the actual spectrum precisely, we further evaluate the measurement using RF modulation as a calibration. Figure 4(a) depicts a phase modulator driven by an RF source that is added before the resonator to generate sidebands. The distance between the sideband and the original signal is used as a ruler to calibrate the x-axis. Figures 4(b)–4(d) demonstrate the calibration process. Initially, we measure resonance without RF modulation. Immediately after, we turn on the RF modulation with an RF frequency of 100 MHz and observe the generation of sidebands. With sidebands as a reference, we calibrate the x-axis, extract the linewidth, and calculate Q values. It is worth noting that although this approach allows one to calibrate the linewidth using a precise RF frequency reference, it underestimates the extinction ratio: sidebands generated by RF signal have nonzero transmission when the laser signal is on resonance with the cavity. The fitting, using simple Lorentzian, then underestimates effective "coupling loss" and thus underestimates intrinsic Q. Care needs to be taken to compensate for this effect. Taking this into account, we evaluate the perceived RF-calibrated loaded Q of 18.39 million, which is comparable to the original loaded Q of 16.07 million.

5. CONCLUSION

We demonstrate microresonators with a record-high intrinsic quality factor of 29 million on monolithic TFLN. We performed statistical analysis of the measured quality factor over different device designs and calibrated the measurement with an RF modulated laser. The optimized design and fabrication process of monolithic TFLN microresonators enable our realization of ultra-high-Q devices. Moving forward, the enhanced high-Q devices on TFLN could substantially improve the device performances of electro-optics and nonlinear photonics, transitioning devices into a new parameter space. This advancement holds great potential to catalyze system-level applications, thus facilitating applications in microwave photonics [54], quantum computing [55,56], and nonlinear optics [57,58]. Our efforts further push the state-of-the-art, showcasing the potential of the TFLN platform and paving the way for future innovative explorations in integrated photonics.

Fig. 4. Resonance calibration with RF-modulated laser light. (a) Schematic of measurement setup incorporating a phase modulator capable of generating optical sidebands. (b) The original resonance without applying RF power exhibits a loaded Q of 16.07 million. (c) Same resonance with sidebands generated by activating the 100 MHz RF sources. (d) Calibration using the sideband positions to redefine the x-axis as frequency and refit the resonance. The loaded Q increases to 18.39 million, slightly higher than the original loaded Q.

REFERENCES

1. D. Zhu, L. Shao, M. Yu, et al., "Integrated photonics on thin-film lithium niobate," Adv. Opt. Photonics **13**, 242–352 (2021).

2. R. S. Weis and T. K. Gaylord, "Lithium niobate: summary of physical properties and crystal structure," Appl. Phys. A **37**, 191–203 (1985).

3. M. Zhang, C. Wang, R. Cheng, et al., "Monolithic ultra-high-Q lithium niobate microring resonator," Optica **4**, 1536–1537 (2017).

4. C. Wang, M. Zhang, X. Chen, et al., "Integrated lithium niobate electro-optic modulators operating at CMOS-compatible voltages," Nature **562**, 101–104 (2018).

5. M. Y. Xu, Y. Zhu, F. Pittalà, et al., "Dual-polarization thin-film lithium niobate in-phase quadrature modulators for terabit-per-second transmission," Optica **9**, 61–62 (2022).

6. Y. Hu, D. Zhu, S. Lu, et al., "Integrated electro-optics on thin-film lithium niobate," arXiv, arXiv:2404.06398 (2024).

7. Y. Hu, M. Yu, D. Zhu, et al., "On-chip electro-optic frequency shifters and beam splitters," Nature **599**, 587–593 (2021).

8. M. Zhang, B. Buscaino, C. Wang, et al., "Broadband electro-optic frequency comb generation in an integrated microring resonator," Nature **568**, 373–377 (2019).

9. Y. Hu, M. Yu, B. Buscaino, et al., "High-efficiency and broadband on-chip electro-optic frequency comb generators," Nat. Photonics **16**, 679–685 (2022).

10. M. Yu, M. Lipson, and T. J. Kippenberg, "Chip-based lithium-niobate frequency combs," IEEE Photonics Technol. Lett. **31**, 1894–1897 (2019).

11. C. Wang, M. Zhang, M. Yu, et al., "Monolithic lithium niobate photonic circuits for Kerr frequency comb generation and modulation," Nat. Commun. **10**, 978 (2019).

12. Z. Lin, Z. Kang, P. Xu, et al., "Turnkey generation of Kerr soliton microcombs on thin-film lithium niobate on insulator microresonators powered by the photorefractive effect," Opt. Express **29**, 42932–42944 (2021).

13. Y. He, Q. F. Yang, J. Ling, et al., "Self-starting bi-chromatic LiNbO₃ soliton microcomb," Optica **6**, 1138–1144 (2019).

14. Z. Gong, X. Liu, Y. Xu, et al., "Near-octave lithium niobate soliton microcomb," Optica **7**, 1275–1278 (2020).

15. Y. Song, Y. Hu, M. Lončar, *et al.*, "Hybrid Kerr-electro-optic frequency combs on thin-film lithium niobate," arXiv, arXiv:2402.11669 (2024).
16. Y. Song, Y. Hu, X. Zhu, *et al.*, "Octave-spanning Kerr soliton micro-combs on thin-film lithium niobate," arXiv, arXiv:2403.01107 (2024).
17. R. Cheng, M. Yu, A. Shams-Ansari, *et al.*, "On-chip synchronous pumped $\chi^{(3)}$ optical parametric oscillator on thin-film lithium niobate," arXiv, arXiv:2304.12878 (2023).
18. Y. Hu, C. Reimer, A. Shams-Ansari, *et al.*, "Realization of high-dimensional frequency crystals in electro-optic microcombs," Optica 7, 1189–1194 (2020).
19. Y. Hu, M. Yu, N. Sinclair, *et al.*, "Mirror-induced reflection in the frequency domain," Nat. Commun. 13, 6293 (2022).
20. U. A. Javid, R. Lopez-Rios, J. Ling, *et al.*, "Chip-scale simulations in a quantum-correlated synthetic space," Nat. Photonics 17, 883–890 (2023).
21. J. Holzgrafe, N. Sinclair, D. Zhu, *et al.*, "Cavity electro-optics in thin-film lithium niobate for efficient microwave-to-optical transduction," Optica 7, 1714–1720 (2020).
22. T. P. McKenna, J. D. Witmer, R. N. Patel, *et al.*, "Cryogenic microwave-to-optical conversion using a triply resonant lithium-niobate-on-sapphire transducer," Optica 7, 1737–1745 (2020).
23. Y. Xu, A. A. Sayem, L. Fan, *et al.*, "Bidirectional interconversion of microwave and light with thin-film lithium niobate," Nat. Commun. 12, 4453 (2021).
24. W. Jiang, C. J. Sarabalis, Y. D. Dahmani, *et al.*, "Efficient bidirectional piezo-optomechanical transduction between microwave and optical frequency," Nat. Commun. 11, 1166 (2020).
25. H. K. Warner, J. Holzgrafe, B. Yankelevich, *et al.*, "Coherent control OFA superconducting qubit using light," arXiv, arXiv:2310.16155v2 (2023).
26. J. Zhao, C. Ma, M. Rüsing, *et al.*, "High quality entangled photon pair generation in periodically poled thin-film lithium niobate waveguides," Phys. Rev. Lett. 124, 163603 (2020).
27. A. Rao, K. Abdelsalam, T. Sjaardema, *et al.*, "Actively-monitored periodic-poling in thin-film lithium niobate photonic waveguides with ultrahigh nonlinear conversion efficiency of 4600 %W^{-1} cm^{-2}," Opt. Express 27, 25920–25930 (2019).
28. C. J. Xin, S. Lu, J. Yang, *et al.*, "Wavelength-accurate and wafer-scale process for nonlinear frequency mixers in thin-film lithium niobate," arXiv, arXiv:2404.12381v1 (2024).
29. P. K. Chen, I. Briggs, C. Cui, *et al.*, "Adapted poling to break the nonlinear efficiency limit in nanophotonic lithium niobate waveguides," Nat. Nanotechnol. 19, 44–50 (2024).
30. X. Li, H. Li, Z. Wang, *et al.*, "Advancing large-scale thin-film PPLN nonlinear photonics with segmented tunable micro-heaters," arXiv, arXiv:2312.09568v2 (2024).
31. S. J. B. Yoo, "Wavelength conversion technologies for WDM network applications," J. Lightwave Technol. 14, 955–966 (1996).
32. G. Wetzstein, A. Ozcan, S. Gigan, *et al.*, "Inference in artificial intelligence with deep optics and photonics," Nature 588, 39–47 (2020).
33. L. Chang, S. Liu, and J. E. Bowers, "Integrated optical frequency comb technologies," Nat. Photonics 16, 95–108 (2022).
34. D. Marpaung, J. Yao, and J. Capmany, "Integrated microwave photonics," Laser Photonics Rev. 7, 506–538 (2013).
35. D. Marpaung, J. Yao, and J. Capmany, "Integrated microwave photonics," Nat. Photonics 13, 80–90 (2019).
36. J. Wang, F. Sciarrino, A. Laing, *et al.*, "Integrated photonic quantum technologies," Nat. Photonics 14, 273–284 (2019).
37. C. C. Wei, J. Li, Q. Jia, *et al.*, "Ultrahigh-Q lithium niobate microring resonator with multimode waveguide," Opt. Lett. 48, 2465–2467 (2023).
38. Y. Gao, F. Lei, M. Girardi, *et al.*, "Compact lithium niobate microring resonators in the ultrahigh Q/V regime," Opt. Lett. 48, 3949–3952 (2023).
39. G. Ulliac, V. Calero, A. Ndao, *et al.*, "Argon plasma inductively coupled plasma reactive ion etching study for smooth sidewall thin film lithium niobate waveguide application," Opt. Mater. 53, 1–5 (2016).
40. K. Prabhakar and R. M. Reano, "Fabrication of low loss lithium niobate rib waveguides through photoresist reflow," IEEE Photonics J. 14, 6660808 (2022).
41. K. Luke, P. Kharel, C. Reimer, *et al.*, "Wafer-scale low-loss lithium niobate photonic integrated circuits," Opt. Express 28, 24452–24458 (2020).
42. A. Kozlov, D. Moskalev, U. Salgaeva, *et al.*, "Reactive ion etching of X-cut LiNbO$_3$ in an ICP/TCP system for the fabrication of an optical ridge waveguide," Appl. Sci. 13, 2097 (2023).
43. F. Kaufmann, G. Finco, A. Maeder, *et al.*, "Redeposition-free inductively-coupled plasma etching of lithium niobate for integrated photonics," Nanophotonics 12, 1601–1611 (2023).
44. R. J. Zhuang, J. He, Y. Qi, *et al.*, "High-Q thin-film lithium niobate microrings fabricated with wet etching," Adv. Mater. 35, 2208113 (2023).
45. F. Yang, X. Fang, X. Chen, *et al.*, "Monolithic thin film lithium niobate electro-optic modulator with over 110 GHz bandwidth," Chin. Opt. Lett. 20, 022502 (2022).
46. R. H. Gao, N. Yao, J. Guan, *et al.*, "Lithium niobate microring with ultra-high Q factor above 10^8," Chin. Opt. Lett. 20, 011902 (2022).
47. J. H. Zhang, R. Wu, M. Wang, *et al.*, "An ultra-high-Q lithium niobate microresonator integrated with a silicon nitride waveguide in the vertical configuration for evanescent light coupling," Micromachines 12, 235 (2021).
48. C. Li, J. Guan, J. Lin, *et al.*, "Ultra-high Q lithium niobate microring monolithically fabricated by photolithography assisted chemo-mechanical etching," Opt. Express 31, 31556–31562 (2023).
49. A. Shams-Ansari, G. Huang, L. He, *et al.*, "Reduced material loss in thin-film lithium niobate waveguides," APL Photonics 7, 081301 (2022).
50. M. W. Puckett, K. Liu, N. Chauhan, *et al.*, "422 million intrinsic quality factor planar integrated all-waveguide resonator with sub-MHz linewidth," Nat. Commun. 12, 934 (2021).
51. G. Moille, Q. Li, T. C. Briles, *et al.*, "Broadband resonator-waveguide coupling for efficient extraction of octave-spanning microcombs," Opt. Lett. 44, 4737–4740 (2019).
52. L. Zhang, L. Jie, M. Zhang, *et al.*, "Ultrahigh-Q silicon racetrack resonators," Photonics Res. 8, 684–689 (2020).
53. M. H. P. Pfeiffer, J. Liu, M. Geiselmann, *et al.*, "Coupling ideality of integrated planar high-Q microresonators," Phys. Rev. Appl. 7, 024026 (2017).
54. J. S. Fandiño, P. Muñoz, D. Doménech, *et al.*, "A monolithic integrated photonic microwave filter," Nat. Photonics 11, 124–129 (2016).
55. E. Pelucchi, G. Fagas, I. Aharonovich, *et al.*, "The potential and global outlook of integrated photonics for quantum technologies," Nat. Rev. Phys. 4, 194–208 (2021).
56. J. L. O'Brien, A. Furusawa, and J. Vučković, "Photonic quantum technologies," Nat. Photonics 3, 687–695 (2009).
57. M. G. Vazimali and S. Fathpour, "Applications of thin-film lithium niobate in nonlinear integrated photonics," Adv. Photonics 4, 034001 (2022).
58. G. Chen, N. Li, J. D. Ng, *et al.*, "Advances in lithium niobate photonics: development status and perspectives," Adv. Photonics 4, 034003 (2022).